Journal of Materials Chemistry A

Large second harmonic generation in penta-CdO_2 sheet exfoliated from its bulk phase

Journal:	*Journal of Materials Chemistry A*
Manuscript ID	TA-ART-09-2022-007589.R1
Article Type:	Paper
Date Submitted by the Author:	11-Nov-2022
Complete List of Authors:	Hou, Changsheng; Peking University Shen, Yiheng; Peking University, College of Engineering Wang, Qian; Peking Univ, Center for Applied Physics and Technology; Peking University, School of Materials Science and Engineering Kawazoe, Yoshiyuki; Tohoku University, New Industry Creation Hatchery Center Jena, Purusottam ; Virginia Commonwealth University, Physics Department

Large second harmonic generation in penta-CdO_2 sheet exfoliated from its bulk phase†

Changsheng Hou,[a] Yiheng Shen,[a] Qian Wang*[a], Y. Kawazoe,[bcd] and P. Jena[e]

[a] CAPT, School of Materials Science and Engineering, BKL-MEMD, Peking University, Beijing, 100871, China.

[b] New Industry Creation Hatchery Center, Tohoku University, Sendai, 980-8577, Japan;

[c] Department of Physics, Suranaree University of Technology, Nakhon Ratchasima, 30000, Thailand;

[d] Department of Physics and Nanotechnology, SRM Institute of Science and Technology, Kattankulathur, Tamil Nadu, 603203, India.

[e] Department of Physics, Virginia Commonwealth University, Richmond, VA, 23284, USA.

* Author to whom any correspondence should be addressed: qianwang2@pku.edu.cn

† Electronic supplementary information (ESI) available.

Abstract

Two-dimensional (2D) materials composed solely of pentagonal motifs are of particular interest due to their unique geometries and novel properties. Especially, the broken centrosymmetry and in-plane mirror symmetry in penta-graphene-like materials result in both the in-plane and out-of-plane second harmonic generation (SHG). Transition metal cations with filled d^{10} shell (d^{10}-TM) can significantly enhance the SHG response as found in many previously studied bulk materials. Here, based on first-principles calculations combined with independent particle approximation, we show that large SHG can also exist in some 2D d^{10}-TM oxides, such as penta-CdO_2, which can be chemically exfoliated from its bulk phase with its dynamical, thermal, and mechanical stability intact. We further find that penta-CdO_2 possesses extraordinary in-plane and out-of-plane SHG response with large static SHG susceptibilities of χsheet 14(0) = χsheet 25(0) = χsheet 36(0) = 8.86 pm^2/V due to the phase-matching between the fundamental and second-harmonic light. In addition, the low thermal expansion and large optical band gap of 3.24 eV endow the penta-CdO_2 sheet with high laser-induced damage threshold. Discussions are also made to the penta-ZnO_2 sheet. This study expands the family of 2D materials with outstanding SHG performance.

Keywords:

Pentagon-based sheet, Second harmonic generation, First-principles calculation

1. Introduction

Nonlinear optics has attracted significant interest due to its important role in photonic applications including ultrafast lasers,[1] frequency conversion,[2] photodetector,[3] and optical modulator/switches/memories.[4] As one of the leading nonlinear optical responses, second harmonic generation (SHG) is one of the hotly pursued topics because it is more easily observed in experiments as compared to other higher-order nonlinear optical effects. In general, SHG materials are non-centrosymmetric and non-metallic. Therefore, the even order terms in their electric polarization expansion can exist ($P = \varepsilon_0\chi^{(2)}E^2 + \varepsilon_0\chi^{(4)}E^4 + \cdots + \varepsilon_0\chi^{(2n)}E^{2n}$). Since the few-atomic thickness of the 2D materials is far below the coherence length of photons, phase-matching condition is usually satisfied, making the SHG response strong enough for observation and utilization.[5] Thus, many non-centrosymmetric 2D materials with large SHG responses have been theoretically predicted and experimentally observed in recent years, including 2H-MoS_2,[6] *h*-BN,[7] 2D CrI_3,[8] 2D GaSe,[9] 2D SnSe,[10] 2D perovskite,[11] α-Sb and α-Bi.[12] In addition, the inversion symmetry of some centrosymmetric bulk materials is broken when thinned down to 2D materials, providing more opportunities to generate SHG response.[13] However, the mirror symmetry in the out-of-plane direction hinders the out-of-plane components of the SHG matrix. For instance, odd-layer MoS_2 sheets with the D_{3h} symmetry possess only one inequivalent in-plane SHG

coefficient.[6] If the out-of-plane mirror symmetry could be broken, the SHG performance would be enhanced. Currently, one of the successful approaches to break the out-of-plane mirror symmetry for a remarkable out-of-plane SHG signal is to construct Janus structures, as is the case with α-In_2Se_3,[14] where the out-of-plane SHG susceptibility spectra enable ultrafast, simple, and noninvasive characterization of the vertical polarization, lattice symmetry, number of layers, and stacking sequence.

Comparing with most 2D non-centrosymmetric materials constructed from the highly symmetric hexagonal motifs, penta-graphene-like materials exhibit both in-plane and out-of-plane SHG response, as found in penta-ZnS_2.[15] Since the theoretical prediction of penta-graphene,[16] over one hundred new pentagonal 2D materials have been theoretically proposed and some experimentally synthesized.[17,18] It is interesting to note that the top-down approach has been successfully used for the synthesis of pentagonal 2D materials. For example, penta-$PdSe_2$ was prepared by exfoliating the bulk $PdSe_2$ in the marcasite phase,[19] and penta-FeS_2 was synthesized by chemically cleaving bulk iron pyrite via liquid-phase exfoliation.[20] Thus, it is important to find new stable pentagonal sheets with extraordinary SHG performance that could potentially be synthesized from marcasite and pyrite materials. Techniques such as chemical vapor deposition[21] and molecular beam epitaxy[22] have also been used in the past to synthesize 2D pentagonal sheets. These include penta-$PdSe_2$, penta-silicene nanoribbon synthesized via physical vapor deposition,[23] penta-PdS_2 fabricated by sulfurization of Pd film,[24] and penta-NiN_2 synthesized using high-pressure approach.[25]

For the application in an optical device, high-quality SHG materials should satisfy

several requirements including high SHG efficiency (a large static SHG susceptibility), moderate birefringence ($0.06 \leq \Delta n \leq 0.1$) to achieve phase-matching, and a high laser-induced damage threshold (LIDT) value in addition to high chemical and physical stabilities and easy-to-synthesize single crystals.[26] Since metal oxides have strong absorption edge, and usually exhibit wide optical band gaps and high LIDT, it has received extensive attention in the design of high-performance SHG materials.[27] Since d^{10}-transition metal (d^{10}-TM) cations (e.g. Zn^{2+}, Cd^{2+}, and Hg^{2+}, etc.) are electron rich, have flexible bonding, and possess polar displacement features, they can be expected to induce much larger polarizability and deformability, stimulating great interest in the design of bulk SHG materials containing d^{10}-TM.[28-32] Thus, it is possible that 2D d^{10}-TM oxides, entirely composed of pentagon motifs, would exhibit large SHG susceptibility, moderate birefringence to achieve phase-matching, and high LIDT. This expectation motivated us to carry out this study.

2. Computational methods

First-principles calculations are performed within the framework of density functional theory (DFT) implemented in the Vienna Ab initio Simulation Package (VASP).[33] The projected augmented wave (PAW)[34] method is used to treat interactions between ion cores and valance electrons. The Perdew–Burke–Ernzerhof (PBE) functional within the generalized gradient approximation (GGA)[35] is used to describe the electronic exchange-correlation interaction. The hybrid Heyd-Scuseria-Ernzerhof (HSE06)[36] functional is further applied to obtain accurate band structures. The energy

cutoff, the convergence thresholds of total energy and inter-atomic force are set to 600 eV, 10^{-8} eV, and 10^{-6} eV·Å^{-1}, respectively. The first Brillouin zone is represented by a 11 × 11 × 1 *k*-point grid using the Monkhorst-Pack scheme.[37] The vacuum space is set to 18.28 Å in the nonperiodic direction to avoid interaction between two adjacent layers. The phonon spectra are calculated using the finite displacement method implemented in the Phonopy code[38] and a 5 × 5 × 1 supercell. The temperature in *ab initio* molecular dynamics (AIMD) simulations is controlled by using the Nosé–Hoover thermostat.[39] The elastic constants are calculated using the finite difference methods.[40]

The SHG susceptibility is described by a third-rank tensor $\chi(2)$ *abc*(−2□, □, □), defined as $P_a(2\omega) = \chi(2)\ abc(-2\square, \square, \square)E_b(\square)E_c(\square)$, where $P(2\omega)$ is the second-order terms of electric polarization, $E(\square)$ is the fundamental light induced electric field, and $a, b, c \in \{x, y, z\}$. The $\chi_{abc}(\omega)$ is calculated within the independent particle approximation[41] by using the package developed by Zhang's group,[42] where the SHG tensor can be expressed by the sum of contributions from the pure inter-band process $\chi_{abc,e}(\omega)$ and the mixed inter-band and intra-band process $\chi_{abc,i}(\omega)$, both of which can be deduced from the electronic structure. The tensor component χbulk $abc(\omega)$ of a bulk material is calculated by

$$\chi_{abc}^{\text{bulk}}(\omega) = \chi_{abc,e}^{\text{bulk}}(\omega) + \chi_{abc,i}^{\text{bulk}}(\omega). \quad (1)$$

Here, χbulk $abc,e(\omega)$ is the contribution from the pure inter-band contribution and has the following form,

$$\chi_{abc,e}^{\text{bulk}}(\omega) = \frac{e^3}{\hbar^2 \Omega} \sum_{nml,k} \frac{r_{nm}^a \{r_{nm}^a r_{ml}^b r_{ln}^c\}}{(\omega_{ln} - \omega_{ml})} \left[\frac{2f_{mn}}{\omega_{mn} - 2\omega} + \frac{f_{ln}}{\omega_{ln} - 2\omega} + \frac{f_{ml}}{\omega_{ml} - \omega} \right]. \quad (2)$$

χbulk $abc,i(\omega)$ is the contribution from the mixed inter-band and intra-band process that

includes the modulation of linear polarization by the intra-band motion (the first three terms), and the intra-band motion modified by the polarization energy associated with inter-band motion of electrons (the last term).

$$\chi^{\text{bulk}}_{abc,i}(\omega) = \frac{\mathrm{i}}{2}\frac{e^3}{\mathrm{h}^2\Omega}\sum_{nm,k} f_{nm}\left[\begin{array}{l} \dfrac{2}{\omega_{mn}(\omega_{mn}-2\omega)} r^a_{nm}(r^b_{nm;c}+r^c_{mn;b}) + \dfrac{1}{\omega_{mn}(\omega_{mn}-\omega)}(r^a_{nm;c}r^b_{mn}+r^a_{nm;b}r^c_{mn}) \\ +\dfrac{1}{\omega^2_{mn}}\left(\dfrac{1}{\omega_{mn}-\omega}-\dfrac{4}{\omega_{mn}-2\omega}\right) r^a_{nm}(r^b_{mn}\Delta^c_{mn}+r^c_{mn}\Delta^b_{mn}) \\ -\dfrac{1}{2\omega_{mn}(\omega_{mn}-2\omega)}(r^b_{nm;a}r^c_{mn}+r^c_{nm;a}r^b_{mn}) \end{array}\right]. \quad (3)$$

Here, Ω is the volume of the periodic cell, $f_{nm} = f_n - f_m$, $\square_{nm} = \square_n - \square_m$, and $\Delta_{nm} = v_{nn} - v_{mm}$ are the differences of the Fermi distribution function, energy, and electron group velocity between the nth and mth bands, respectively. The operator *ra mn* = *pa mn*/*im*ω_{mn} is the position operator r_{mn} projected on axial directions, which can be derived from the momentum matrix component p_{mn}. {*rb nlra lm*} is defined as 1/2(*rb nlra lm*+ *ra nlrb lm*). *rb nm;a* is the generalized derivative of the coordinate operator in momentum space and has the form,

$$r^b_{nm;a} = \frac{r^a_{nm}\Delta^b_{mn} + r^b_{nm}\Delta^a_{mn}}{\omega_{nm}} + \frac{\mathrm{i}}{\omega_{nm}}\sum_l(\omega_{lm}r^a_{nl}r^b_{lm} - \omega_{nl}r^b_{nl}r^a_{lm}). \quad (4)$$

The static SHG susceptibility can be obtained by the Kramers-Kronig transformation,[43]

$$\chi^{\text{bulk}}_{abc}(0) = \mathrm{Re}[\chi^{\text{bulk}}_{abc}(0)] = \frac{2}{\pi}P\int_0^\infty \{\mathrm{Im}[\chi^{\text{bulk}}_{abc}(\omega)]/\omega]\}d\omega. \quad (5)$$

To obtain the converged SHG susceptibility tensor, the electronic structures are calculated at the PBE level with a very dense k-point sampling of 99 × 99 × 1. Since

the PBE/GGA underestimates the band gap in the calculation of optical properties, the scissor approximation is applied where the difference between the band gaps is obtained at the PBE and HSE06 levels in SHG calculations.[44] For 2D materials, it is necessary to replace the volume Ω in equations (2) and (3) with the area of the 2D plane of the unit cell, as the volume depends on the thickness of the vacuum space in the normal direction of 2D materials.[10] Thus, the unit of the sheet SHG susceptibility χsheet *abc* is pm^2/V.

The linear optical properties of bulk materials are obtained from the complex frequency-dependent dielectric function εbulk $ij(\omega)$. The imaginary part Im[εbulk $ij(\omega)$] is calculated by the following equation:[45]

$$\mathrm{Im}[\varepsilon_{ij}^{\mathrm{bulk}}(\omega)] = \frac{2e^2\pi}{\Omega\varepsilon_0}\sum_{k,v,c}\left|<\psi_k^c|\hat{u}\times r|\psi_k^v>\right|^2\delta(E_k^c - E_k^v - E). \quad (6)$$

Here, u and e represent the incident electric field and elementary charge, while $\psi c\ k$ and $\psi v\ k$ denote the conduction band and valence band wave function at the given k point, respectively. The real part Re[εbulk $ij(\omega)$] is obtained from the imaginary part based on the Krammer–Krong dispersion relation:[46]

$$\mathrm{Re}[\varepsilon_{ij}^{\mathrm{bulk}}(\omega)] = 1 + \frac{2}{\pi}P\int_0^{\infty}\frac{\omega'^2\,\mathrm{Im}[\varepsilon_{ij}^{\mathrm{bulk}}(\omega)]}{\omega'^2-\omega^2}d\omega'. \quad (7)$$

Here, P denotes the principal value.

The real and imaginary dielectric functions of 2D materials also need to be renormalized due to the thickness-dependent volume Ω in equation (6). Therefore, we use the following formulas[47] to calculate the dielectric functions of the penta-CdO_2 sheet εsheet $ij(\omega)$:

$$\mathrm{Re}[\varepsilon_{ij}^{\mathrm{sheet}}(\omega)] = 1 + \frac{L_z}{L_z^{eff}}\{\mathrm{Re}[\varepsilon_{ij}^{\mathrm{bulk}}(\omega)] - 1\}. \quad (8)$$

$$\mathrm{Im}[\varepsilon_{ij}^{\mathrm{sheet}}(\omega)] = \frac{L_z}{L_z^{eff}}\mathrm{Im}[\varepsilon_{ij}^{\mathrm{bulk}}(\omega)]. \quad (9)$$

Here, L_z is the cell length along the normal direction of the sheet, and *Leff z* is the effective length, and is determined by the sum of the van der Waals thickness (3.4 Å on each side of the sheet) and the thickness (d_{2D}) of the 2D material via the equation, *Leff z* = 3.4 Å × 2 + d_{2D}. Tests for the thickness-independent of our calculated SHG susceptibility and dielectric function are carried out. The details can be found in Fig. S1 in the ESI.

3. Results and discussion

3.1 Structure and stability

The 2D frameworks featuring the Cairo pentagonal tessellation exist in the marcasite and pyrite materials with the *Pbca* symmetry (space group No. 61) and $Pa\bar{3}$ symmetry (space group No. 206), respectively.[48] Hence, it is possible to obtain the corresponding pentagon-based sheets by using physical or chemical exfoliation technique. We rationally search for pentagonal d^{10}-TM oxide sheets from their bulk counterparts containing internal pentagonal layers. The searching starts from an initial set of crystals extracted from the Materials Project (MP) Database,[49] retrieving entries with one d^{10}-TM element and oxygen, where we only consider the compounds matching the experimentally determined materials in the Inorganic Crystal Structure Database (ICSD).[50] Under these conditions, the initial dataset provides 45 bulk structures for

further analysis, as summarized in Table S1 in the ESI. Then, according to the features of the marcasite and pyrite unit cells, we use the space group symmetry (*Pbca* or *Pa* $\bar{3}$), the stoichiometry (1:2 or 2:1), and 12 atoms per unit cell as descriptors to identify bulk materials with marcasite or pyrite configuration. These combined criteria reduce the original set of the 45 bulk structures to 2 pyrite structures (ZnO_2 and CdO_2) and 1 marcasite structure (HgO_2). We then directly extract pentagonal sheets from the bulk materials. The fully optimized geometries of the pentagonal sheets extracted from bulk ZnO_2 and CdO_2 exhibit the penta-graphene-like configuration with $P\bar{4}2_1m$ symmetry (space group No. 113), which are termed as penta-ZnO_2 and penta-CdO_2, respectively. The fully optimized pentagonal sheet extracted from bulk HgO_2 possesses the penta-$PdSe_2$-like[19] configuration with $P2_1/c$ symmetry (space group No. 14), which is named penta-HgO_2. In the next step, we calculate their phonon spectra to check their dynamic stabilities. The results plotted in Fig. S2 show that penta-ZnO_2, penta-CdO_2 and penta-HgO_2 are all dynamically stable as no any imaginary modes are found in the first Brillouin Zones of their phonon spectra. Only the penta-graphene-like configuration of pentagon-based sheets can exhibit both in-plane and out-of-plane SHG response.[15] The other two typical types including penta-$PdSe_2$-like and penta-NiN_2-like[25] configurations are centrosymmetric, which do not meet the basic requirements of exhibiting SHG, thus reducing the original set of the three structures to two stable structures, namely, penta-ZnO_2 and penta-CdO_2. Since the difference in electronegativity of Cd and O atoms (1.75) is smaller than that of Zn and O atoms (1.79), the Cd-O bond is more covalent than the Zn-O bond, and the electrons in the Cd-O

bond are expected to exhibit a stronger response under the electric field than that in the Zn-O bond, implying a stronger SHG response in penta-CdO_2. Hence, we choose the penta-CdO_2 sheet for further investigation. More details on penta-ZnO_2 can be found in electronic supplementary information (ESI).

The optimized geometry and phonon spectrum of the penta-CdO_2 sheet are presented in Fig. 1(a-b). The unit cell contains two Cd and four O atoms, which occupy two nonequivalent Wyckoff positions, namely, 2b (0.500, 0.500, 0.500) and 4e (0.605, 0.105, 0.543), respectively. Its lattice parameters are $a = b = 5.00$ Å. The Cd-O, and O-O bond lengths are 2.22 Å and 1.49 Å, respectively. The buckling height of the penta-CdO_2 sheet is 1.72 Å. To explore the feasibility of its experimental synthesis, we calculate the exfoliation energies of the monolayer and bilayer penta-CdO_2, which are defined as

$$E_{\mathrm{exf}}(n) = [E_{\mathrm{iso}}(n) - \frac{n}{m} E_{\mathrm{bulk}}] / A . \quad (10)$$

Here, $E_{\mathrm{exf}}(n)$, $E_{\mathrm{iso}}(n)$, and E_{bulk} denote the exfoliation energy, the energy of the exfoliated sheet, and the energy of the bulk material, respectively. The parameters n, m and A are the number of layers in the exfoliated sheet and the bulk material, and the surface area of the bulk material, respectively. The calculated exfoliation energies of the monolayer and bilayer penta-CdO_2 are 0.85 J m^{-2} and 0.12 J m^{-2}, which are comparable to those of graphene[51] (0.37 J m^{-2}) and phosphorene[52] (0.35 J m^{-2} for the monolayer and 0.37 J m^{-2} for the bilayer), indicating that it is possible to obtain the penta-CdO_2 sheet from its bulk counterpart.

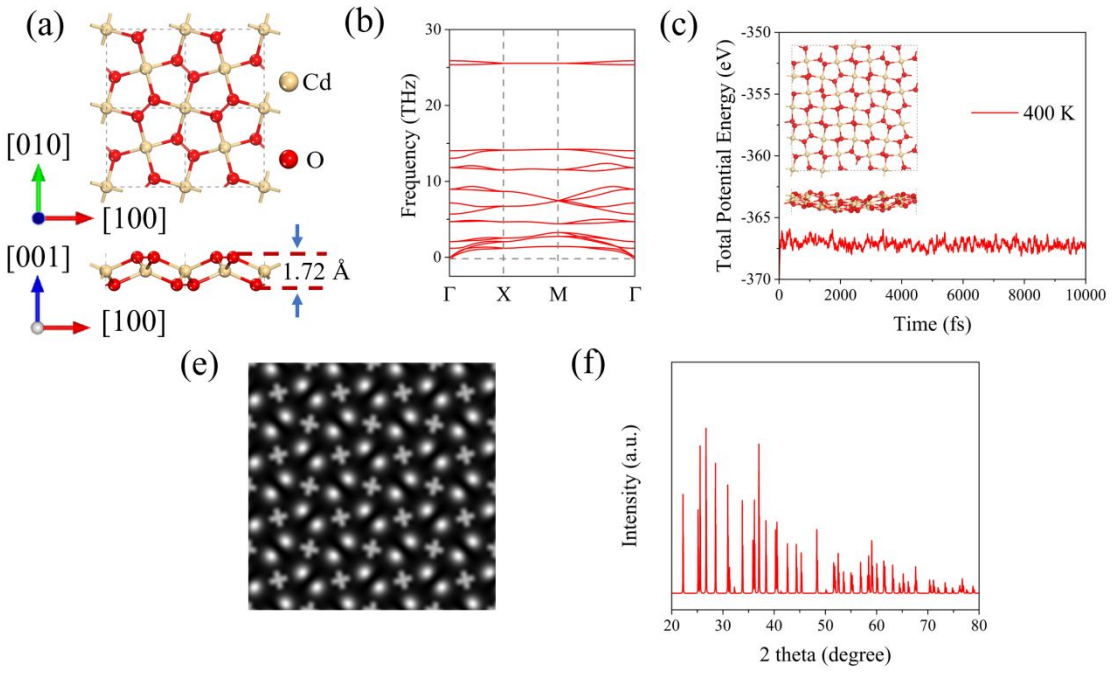

Fig. 1 (a) Top and side views of the optimized geometry, and (b) phonon spectrum of penta-CdO_2. (c) Total potential energy fluctuation of penta-CdO_2 with time during the AIMD simulation at 400 K. (d) Simulated constant height STM image with bias voltage $V_{bias} = -1$ mV, and (e) simulated XRD pattern of the penta-CdO_2 sheet.

The thermal stability of penta-CdO_2 is examined by performing AIMD simulations at 400 K. The duration of the simulation is 10 ps with a time step of 1 fs. To ensure that the observed stability is not caused by the constraints of periodic boundary conditions, a 4 × 4 × 1 supercell is used in the simulations. As shown in Fig. 1(c), the total potential energy fluctuates slightly around a constant value during the simulation and the geometry does not suffer significant distortion at the end of the simulation, which indicates that the penta-CdO_2 sheet is thermally stable at 400 K.

The simulated scanning tunneling microscopy (STM) image is graphically plotted in Fig. 1(d). One can see that some O-O dimers are brighter than the others, reflecting

the buckled feature of this sheet. The simulated X-Ray diffraction (XRD) of penta-CdO_2 is also carried out, which is presented in Fig. 1(e). Finally, we examine the mechanical stability of penta-CdO_2. The calculated linear elastic constants are C_{11} = 28.67 N m^{-1}, C_{12} = –0.86 N m^{-1}, and C_{66} = 13.72 N m^{-1}. These values satisfy the requirements of Born-Huang criteria,[53] namely, $C_{11} > 0$, $C_{11} > C_{12}$ and $C_{66} > 0$ for 2D materials, confirming that penta-CdO_2 is mechanically stable.

3.2 Mechanical properties

Having confirmed the stability of penta-CdO_2, we study the mechanical properties of penta-CdO_2 based on its linear elastic constants. The in-plane Young's modulus (E) and Poisson's ratio (ν) along an arbitrary direction (θ) are deduced from the following formulas:[54]

$$E(\theta) = \frac{C_{11}^{\ 2} - C_{12}^{\ 2}}{C_{11}(s^4 + c^4) + (\frac{C_{11}^{\ 2} - C_{12}^{\ 2}}{C_{66}} - 2C_{12})c^2 s^2}, \quad (11)$$

$$\nu(\theta) = -\frac{(2C_{11} - \frac{C_{11}^{\ 2} - C_{12}^{\ 2}}{C_{66}})c^2 s^2 - C_{12}(c^4 + s^4)}{C_{11}(s^4 + c^4) + (\frac{C_{11}^{\ 2} - C_{12}^{\ 2}}{C_{66}} - 2C_{12})c^2 s^2}. \quad (12)$$

Here, $s = \sin\theta$, $c = \cos\theta$, and θ represents the in-plane angle with respect to the [100] direction. As shown in Fig. 2(a), the Young's modulus E shows weak anisotropy, and its maximum value is 28.64 N m^{-1} along the [100] direction, which is only about 8% of that of graphene (345 N m^{-1}).[55] The Poisson's ratio ν of penta-CdO_2 is highly anisotropic, exhibiting butterfly-like characteristics. Interestingly, we note that C_{12} is negative for penta-CdO_2, leading to a negative Poisson's ratio (NPR) along most

directions. The largest value of positive Poisson's ratio is 0.01 along the [110] and its equivalent directions. While, the largest absolute value of negative Poisson's ratio is –0.03 along the [100] and its equivalent directions. Therefore, penta-CdO_2 with NPR may have applications in nanomechanical devices as a nano-auxetic material.

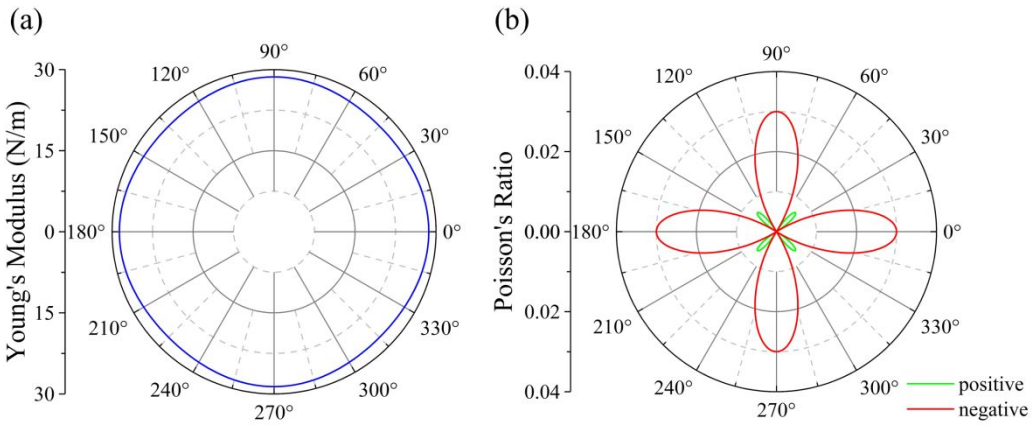

Fig. 2 Variation of (a) the in-plane Young's modulus, and (b) Poisson's ratio with the direction in penta-CdO_2.

3.3 Electronic properties

The electronic properties of penta-CdO_2 are studied by calculating its band structure and corresponding total and partial density of states (DOS) at the HSE06 level, the results are plotted in Fig. 3(a). The band structure calculated at the PBE level is also given for comparison. One can see that penta-CdO_2 is semiconducting with an indirect bandgap of 1.54 eV at the PBE level, as the valance band maximum (VBM) and conduction band minimum (CBM) are located at the different points along the M-Γ path in the first Brillouin zone. The electronic band structure at the HSE06 level has a similar dispersion but with a larger band gap of 3.28 eV due to the well-known fact that

the PBE functional underestimates the band gaps. The partial DOS (PDOS) shows that the VBM is mainly contributed by the O atoms, while the CBM comes from both the Cd and O atoms.

Next, we calculate the electron localization function (ELF)[56] for this sheet. The ELF is a dimensionless parameter normalized in the range [0.0, 1.0], where 0.0 corresponds to a low electron density, 1.0 corresponds to fully localized electrons and 0.5 corresponds to completely delocalized electrons, as shown in Fig. 3(b). One can see that the ELF values in the vicinity of the O-O dimers (yellow and orange cloud) are in between 0.5 and 1.0, indicating these electrons exhibit covalent nature. That the free electrons (green cloud) surrounding the O-O dimers are separated by the blue regions with low charge density further confirm the semiconducting feature of the penta-CdO_2 sheet. Using the Bader charge analysis,[57,58] we find that each Cd atom transfers 1.21 electrons to each of the O-O dimer, which is larger than that in penta-ZnS_2 sheet[15] (0.88 electrons). Hence, the electrons of O-O dimers in penta-CdO_2 are more delocalized than those of S-S dimers in penta-ZnS_2, indicating the electrons of O-O dimers can exhibit a more obvious response under an electric field, leading to a strong SHG response in penta-CdO_2.

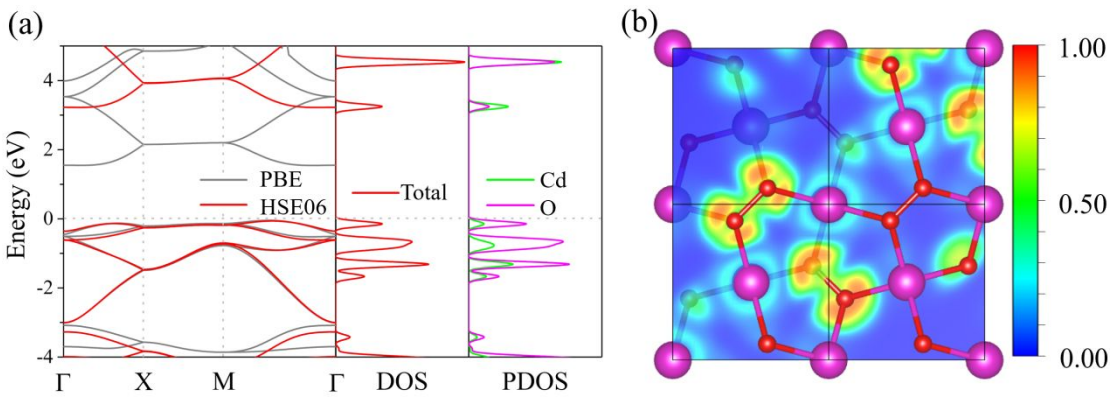

Fig. 3 (a) Electronic band structure, total and partial DOS of penta-CdO_2. (b) ELF distribution on the plane formed by the ∠O-O-Cd in penta-CdO_2.

3.4 SHG susceptibility

We then evaluate the SHG properties of penta-CdO_2. Because the penta-CdO_2 sheet belongs to $P\bar{4}2_1m$ symmetry (space group No. 113), only two independent nonzero components χsheet $xyz(\omega)$ = χsheet $yxz(\omega)$ and χsheet $zxy(\omega)$ are allowed by the symmetry constraints, which are further reduced to χsheet $14(\omega)$ = χsheet $25(\omega)$ and χsheet $36(\omega)$ under Voigt notation.[59] These tensor components show a crossover between the direction of SHG response and the incident electric field, where the out-of-plane electric field contributes to the in-plane polarization via χsheet $14(\omega)$ and χsheet $25(\omega)$, and the in-plane electric field is also necessary for the out-of-plane polarization via χsheet $36(\omega)$. Hence, penta-CdO_2 can exhibit both in-plane and out-of-plane SHG susceptibilities. To compensate for the underestimated band gap at the PBE level, we use the scissor correction of the band gap difference Δ = 1.74 eV in the calculations of the SHG for higher accuracy.[44] Besides, we find that the SHG properties converge at a k-point mesh of 99 × 99 × 1, which is illustrated in Fig. S3.

Next, we calculate the static SHG susceptibilities of penta-CdO_2, which are the

zero-frequency limit of the SHG susceptibilities. The static SHG susceptibilities satisfy Kleiman's symmetry, where only one independent value χsheet 14(0) = χsheet 25(0) = χsheet 36(0) = 8.86 pm^2/V exists in penta-CdO_2, which is much larger than that of penta-ZnS_2 [χsheet 14(0) = χsheet 36(0) = –1.22 pm^2/V, χsheet 31(0) = χsheet 15(0) = 0.69 pm^2/V].[15] In addition, to compare with the results of the SHG of bulk materials, the sheet SHG susceptibility χsheet $abc(\omega)$ of 2D materials can be converted to the corresponding bulk SHG susceptibility χbulk $abc(\omega)$ via the equation χsheet $abc(\omega)$ = χbulk $abc(\omega) \times$ *Leff z*, where *Leff z* is the effective length used for the correction of dielectric function. The converted static bulk SHG susceptibility χbulk 14(0) = χbulk 25(0) = χbulk 36(0) of penta-CdO_2 is 1.04 pm/V, which is about twice larger than that of the well-known KBBF [experimental value of 0.47 pm/V at the low photon energy of ω = 1.17 eV,[60] while our calculated value is 0.45 pm/V, as presented in Fig. S4 in the ESI]. Such large static SHG susceptibility indicates a strong frequency-doubling effect in penta-CdO_2, which is promising for optical device applications.

To study the thickness dependence of the SHG of penta-CdO_2, we carry out calculations for the bilayer and trilayer penta-CdO_2 sheets using the Grimme's semiempirical van der Waals correction (DFT-D3).[61] The AA-stacking configuration is found to be the most stable for the bilayer penta-CdO_2 sheet (see Fig. S5). On the other hand, the optimized trilayer penta-CdO_2 (see Fig. S6) undergoes a phase transition toward its bulk pyrite phase without SHG response due to the $Pa\bar{3}$ centro-symmetry with the space group of No. 206. Thus, we only focus on the bilayer configuration. The static SHG susceptibility of bilayer penta-CdO_2 is calculated to be χsheet 14(0) = χsheet

25(0) = χsheet 36(0) =13.17 pm^2/V, which is larger than the value of the penta-CdO_2 sheet [χsheet 14(0) = χsheet 25(0) = χsheet 36(0) = 8.86 pm^2/V]. The calculated results for the SHG susceptibility of the bilayer penta-CdO_2 sheet are plotted in Fig. S7 in the ESI.

Next, we calculate the frequency-dependent SHG susceptibility of penta-CdO_2, especially considering its imaginary part (Im[χsheet $abc(\omega)$]). The imaginary parts of different nonzero independent SHG tensor components are plotted in Fig. 4, while the real parts and modulus are plotted in Fig. S8. Unlike previously reported 2D materials with major in-plane SHG response,[10] the penta-CdO_2 sheet has both strong in-plane and out-of-plane SHG responses. One can see that Im[χsheet 14(ω)] and Im[χsheet 36(ω)] have the most significant peak value of 264.12 pm^2/V and 368.92 pm^2/V at 1.88 eV, respectively. From equation (5), it can be inferred that the low-energy region of Im[χsheet $abc(\omega)$] primarily determines the value of χsheet abc(0) due to the existence of denominator ω in integrand. Hence, the first several peaks in Im[χsheet $abc(\omega)$] make the dominant contributions to χsheet abc(0). For reference, the most significant peak Im[χsheet 36(ω)] value in penta-ZnS_2 is −13.76 pm^2/V at 3.19 eV, which is pushed away from the low energy range due to its larger band gap of 3.34 eV. Thus, the larger value of the most significant peak in penta-CdO_2 and its larger contribution lead to a larger χsheet abc(0) value as compared to that in penta-ZnS_2. In addition, all of the major peaks in Im[χsheet $abc(\omega)$] of penta-CdO_2 are located within the photon energy range of 1.63 ~ 3.10 eV (400 ~ 760 nm), showing good visible nonlinear optical properties.

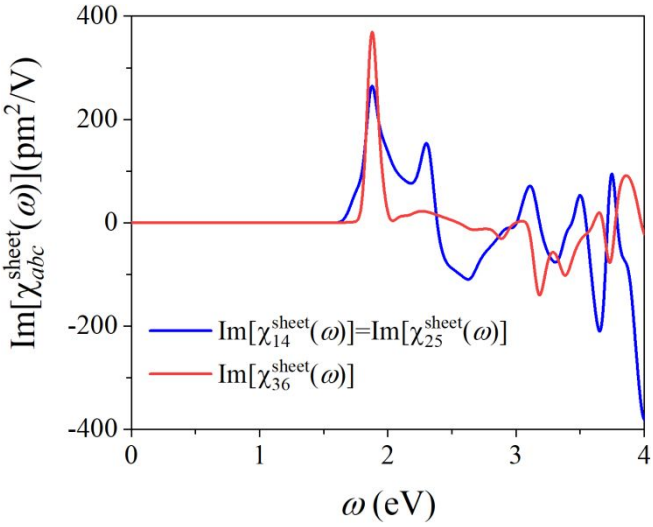

Fig. 4 Imaginary part of the SHG susceptibilities of penta-CdO_2.

For the SHG response in a semiconductor, the light-induced electric polarization ($P = \Sigma p + \int j dt$) includes two main physical contributions, which are the inter-band contribution (A dipole moment p created by pure inter-band transition) and intra-band contribution (A polarization current j generated by electrons moving within their original bands driven by the E-field). We calculate the contribution from different mechanisms to the Im[χsheet $abc(\omega)$] of penta-CdO_2. In Fig. 5(a-b), we plot the different contributions to the imaginary part of SHG in penta-CdO_2. We see that the inter-band and intra-band contributions to each SHG susceptibility tend to oppose each other, and the major peaks are mostly contributed by the intra-band term. Hence, the intra-band contribution to each SHG susceptibility is larger in magnitude compared to that from inter-band contribution.

We then calculate the imaginary part of the dielectric function Im[εsheet $xx(\omega/2)$] and Im[εsheet $zz(\omega/2)$] at the PBE level using the identical k-point mesh in the SHG

calculations. The calculated results are plotted in Fig. 5(c-d). To explore the connection between the SHG property and the linear optical property of penta-CdO_2, the mutual extrema in Im[χsheet $abc(\omega)$] and Im[εsheet $ij(\omega/2)$] are marked in Fig. 5 by the dashed lines. One can see that the major peak of Im[χsheet 14(ω)] and Im[χsheet 36(ω)] at 1.88 eV is related to both Im[εsheet $xx(\omega/2)$] and Im[εsheet $zz(\omega/2)$]. On the other hand, the minor peak of Im[χsheet 14(ω)] at 2.35 eV is related to Im[εsheet $xx(\omega/2)$]. Because SHG is a two-photon process, the incident light with frequencies of both 2ω and ω can induce resonance for band energy difference of $2\hbar\omega$. For penta-CdO_2, the spectra of Im[εsheet $ij(\omega/2)$] exhibits significant absorption peaks at ω = 3.76, 4.70, and 6.40 eV, respectively. Hence, the peaks in Im[χsheet $abc(\omega)$] at ω = 1.88, 2.35, and 3.20 eV are induced by two-photon resonance, indicating a strong SHG response. Meanwhile, the k-point-dependent distributions of dielectric functions are used to analyze the connection between the SHG property and the band structure, which are illustrated in Fig. S9. Here, we focus on the peaks of Im[εsheet $xx(\omega/2)$] and Im[εsheet $zz(\omega/2)$] at $\omega/2$ = 1.88 eV, which are both relevant to that of Im[χsheet 14(ω)] and Im[χsheet 36(ω)]. One can see that the main contributions to Im[εsheet $xx(\omega/2)$] and Im[εsheet $zz(\omega/2)$] are from the transitions at the high symmetry point M and M-Γ path. We further decompose the summed-up contribution from all band-to-band transitions at each k-point to particular band-to-band transitions. The major contribution to the peak value of Im[εsheet $xx(\omega/2)$] is from the degenerate VBM-2-CBM and VBM-3-CBM+1 transitions at the high symmetry point M, and that of Im[εsheet $zz(\omega/2)$] is mainly from the VBM-2-CBM transition along the M-Γ path. These are marked by pink and green

arrows in Fig. S9(c). It is also worth mentioning that the excited electron tends to transfer from the negatively charged O atoms to the positively charged Cd atoms, as shown in the band decomposed charge density in Fig. S10, implying that the electronic states of the Cd-O bonds are the origin of the strong SHG susceptibility of penta-CdO_2.

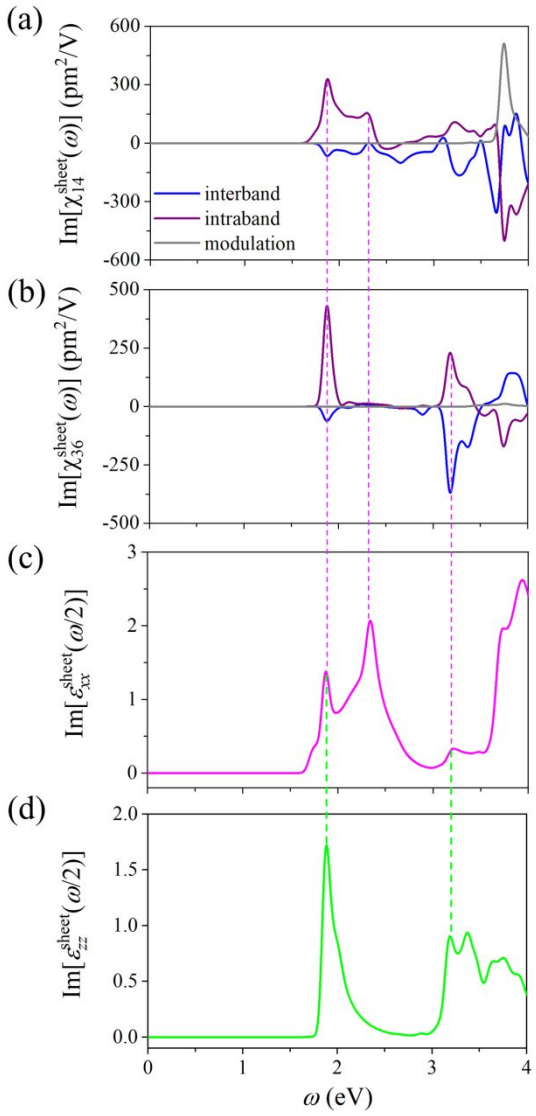

Fig. 5 Imaginary parts (a) Im[χsheet 14(ω)] and (b) Im[χsheet 36(ω)] of the inter-band, intra-band and modulation for the SHG susceptibility, and imaginary part of the dielectric function (c) Im[εsheet xx(ω/2)] and (d) Im[εsheet zz(ω/2)] of penta-CdO_2.

3.5 Phase-matching

In addition to the SHG susceptibility, the phase-matching is another crucial factor for high-quality SHG materials. This is closely related to the incident laser wavelength.[62] To show the phase-matching behavior of penta-CdO_2, we calculate the refractive index n and birefringence Δn by using the previously calculated dielectric function ε_{xx} and ε_{zz}. Refractive index n is obtained according to the formula:[63]

$$n_{ij}(\omega) = \frac{1}{\sqrt{2}}\left[|\varepsilon_{ij}^{\text{sheet}}(\omega)| + \text{Re}[\varepsilon_{ij}^{\text{sheet}}(\omega)] \right]^{\frac{1}{2}}. \quad (13)$$

Here, i, j = 1, 2, 3 correspond to the x, y, and z directions of the Cartesian coordinates and Re[εsheet $xx(\omega)$] and Im[εsheet $xx(\omega)$] are the real and imaginary parts of dielectric function, respectively. Besides, birefringence (Δn) is calculated as Δn = max $|n_i - n_j|$, $i \neq j$. As shown in Fig. 6(a), the calculated refractive indices (n) indicate that the $n_z(n_e)$ values of penta-CdO_2 are smaller than $n_x = n_y(n_o)$, where n_x, n_y, and n_z are the refractive indices along the x, y, and z directions, and n_e and n_o are refractive indices of extraordinary and ordinary light, respectively. Hence, the penta-CdO_2 sheet is a negative uniaxial crystal. On the basis of the type-I phase-matching conditions of $n_e(2\omega) = n_o(\omega)$, where ω and 2ω refer to fundamental and second-harmonic light, respectively, the wavelength limits for penta-CdO_2 is 682 nm, which occurs in the visible light range. One can see that the birefringence is around 0.06 in Fig. 6(b), exhibiting moderate birefringence ($0.06 \leq \Delta n \leq 0.1$).[26] This indicates that the fundamental and second-harmonic light exhibit phase-matching when propagating in this sheet, so that the SHG response can be enhanced. As generally accepted, the laser-induced damage threshold of a material is influenced by several factors, including optical band gap, thermal

expansion, physical and chemical stability, crystal quality, etc.[64] Among these, the optical band gap is generally the main factor for both single crystal and polycrystalline samples.[62] As shown in Fig. S11(a), we use Tauc plot methodology to obtain the optical band gap of the penta-CdO_2 sheet, which is shown as follows:[65]

$$(\alpha h\nu)^n = K(h\nu - E_g). \quad (14)$$

In this equation, α is the absorption coefficient, $h\nu$ is the incident photon energy, K is an energy independent constant, and E_g is the optical band gap. Besides, for direct band gap material $n = 2$, while for indirect $n = 1/2$. The calculated optical band gap of penta-CdO_2 is 3.24 eV, indicating high LIDT for penta-CdO_2. Note that only the SHG signal below the minimal band pair energy of 3.24 eV is considered in the above analysis, because of the dominant linear optical absorption beyond this limit. We also calculate the thermal expansion from 0 K to 400 K of penta-CdO_2 by using the quasi harmonic approximation method[66] as implemented in the Phonopy code.[38] The results are plotted in Fig. S11(b). The low thermal expansion also favors its high LIDT.

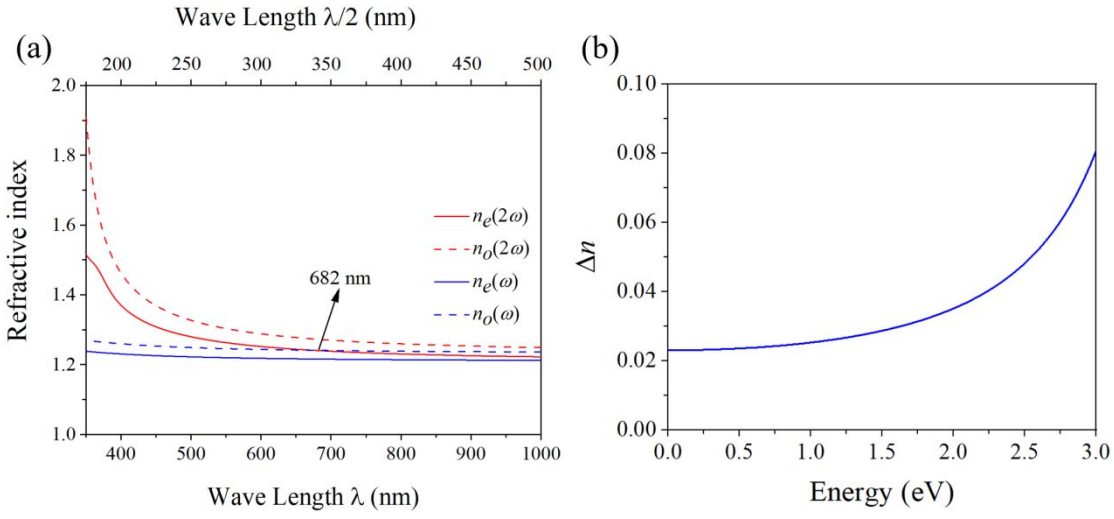

Fig. 6 (a) Wavelength-dependent refractive indices and (b) energy-dependent

birefringence of penta-CdO_2.

4. Conclusions

In summary, the SHG performance of 2D d^{10}-TM oxides, the penta-CdO_2 sheet, is studied for the first time using first-principles calculations combined with independent particle approximation. We show that the penta-CdO_2 sheet can be chemically exfoliated from its bulk phase with a low exfoliation energy of 0.85 J m^{-2}, and is dynamically, thermally and mechanically stable. Penta-CdO_2 is semiconducting with an indirect band gap of 3.28 eV at the HSE06 level, and possesses a negative Poisson's ratio of $\nu_{12} = \nu_{21} = C_{12}/C_{11} = -0.03$. More interestingly, it exhibits both in-plane and out-of-plane static SHG susceptibilities with the value of χsheet 14(0) = χsheet 25(0) = χsheet 36(0) = 8.86 pm^2/V, which is larger than that of penta-ZnS_2 [χsheet 14(0) = χsheet 36(0) = –1.22 pm^2/V, χsheet 31(0) = χsheet 15(0) = 0.69 pm^2/V]. The Im[χsheet 14(ω)] and Im[χsheet 36(ω)] have the most significant peak values of 264.12 pm^2/V and 368.92 pm^2/V at 1.88 eV, respectively, showing good visible nonlinear optical properties. The low thermal expansion together with a large optical band gap of 3.24 eV makes penta-CdO_2 promising for high laser-induced damage threshold. In addition, we extend to this study to the penta-ZnO_2 sheet, another 2D d^{10}-TM oxide, which also exhibits large SHG response: χsheet 14(0) = χsheet 25(0) = χsheet 36(0) = –5.60 pm^2/V. We hope that these intriguing features will stimulate experimental efforts in the synthesis of such 2D pentagonal materials for the applications in nano SHG devices.

ASSOCIATED CONTENT

*Supporting Information on the forty-five d^{10}-TM oxides from the Materials Project (MP) Database, phonon spectra; SHG susceptibility, band-decomposed charge density distribution, optical band gap, optimized geometry, and electronic band structure.

Conflicts of interest

There are no conflicts to declare.

Acknowledgments

This work is partially supported by grants from the National Natural Science Foundation of China (Grant Nos. NSFC-11974028) and NSFC-12274007, the Ministry of Science and Technology of China (Grant No. 2021YFB4000601), and is also supported by the High-Performance Computing Platform of Peking University, China. P. J. acknowledges partial support by the U.S. Department of Energy, Office of Basic Energy Sciences, Division of Materials Sciences and Engineering under Award DE-FG02-96ER45579. The authors thank the crew of the Center for Computational Materials Science, the Institute for Materials Research, Tohoku University (Japan) for their continuous support of the MASAMUNE-IMR supercomputing facility.

References

1 U. Keller, Recent developments in compact ultrafast lasers, *Nature*, 2003, **424,** 831-838.
2 D. Cyranoski, Materials science: China's crystal cache, *Nature*, 2009, **457,** 953-955.
3 F. Zhou, I. Abdelwahab, K. Leng, K. P. Loh and W. Ji, 2D Perovskites with giant

excitonic optical nonlinearities for high-performance sub-bandgap photodetection, *Adv. Mater.*, 2019, **31,** 1904155.

4 Z. Sun, A. Martinez and F. Wang, Optical modulators with 2D layered materials, *Nat. Photonics*, 2016, **10,** 227-238.

5 M. Zhao, Z. Ye, R. Suzuki, Y. Ye, H. Zhu, J. Xiao, Y. Wang, Y. Iwasa and X. Zhang, Atomically phase-matched second-harmonic generation in a 2D crystal, *Light Sci. Appl.*, 2016, **5,** e16131.

6 Y. Li, Y. Rao, K. F. Mak, Y. You, S. Wang, C. R. Dean and T. F. Heinz, Probing symmetry properties of few-layer MoS_2 and h-BN by optical second-harmonic generation, *Nano Lett.*, 2013, **13,** 3329-3333.

7 C. J. Kim, L. Brown, M. W. Graham, R. Hovden, R. W. Havener, P. L. McEuen, D. A. Muller and J. Park, Stacking order dependent second harmonic generation and topological defects in h-BN bilayers, *Nano Lett.*, 2013, **13,** 5660-5665.

8 Z. Sun, Y. Yi, T. Song, G. Clark, B. Huang, Y. Shan, S. Wu, D. Huang, C. Gao, Z. Chen, M. McGuire, T. Cao, D. Xiao, W. T. Liu, W. Yao, X. Xu and S. Wu, Giant nonreciprocal second-harmonic generation from antiferromagnetic bilayer CrI_3, *Nature*, 2019, **572,** 497-501.

9 X. Zhou, J. Cheng, Y. Zhou, T. Cao, H. Hong, Z. Liao, S. Wu, H. Peng, K. Liu and D. Yu, Strong second-harmonic generation in atomic layered GaSe, *J. Am. Chem. Soc.*, 2015, **137,** 7994-7997.

10 H. Wang and X. Qian, Giant optical second harmonic generation in two-dimensional multiferroics, *Nano Lett.*, 2017, **17,** 5027-5034.

11 W. J. Wei, X. X. Jiang, L. Y. Dong, W. W. Liu, X. B. Han, Y. Qin, K. Li, W. Li, Z. S. Lin, X. H. Bu and P. X. Lu, Regulating second-harmonic generation by van der waals interactions in two-dimensional lead halide perovskite nanosheets, *J. Am. Chem. Soc.*, 2019, **141,** 9134-9139.

12 Y. Guo, H. Zhu and Q. Wang, Large second harmonic heneration in elemental α-Sb and α-Bi monolayers, *J. Phys. Chem. C*, 2020, **124,** 5506-5513.

13 F. Liu, W. Wu, Y. Bai, S. H. Chae, Q. Li, J. Wang, J. Hone and X. Y. Zhu, Disassembling 2D van der waals crystals into macroscopic monolayers and reassembling into artificial lattices, *Science*, 2020, **367,** 903-906.

14 L. Hu and X. Huang, Peculiar electronic, strong in-plane and out-of-plane second harmonic generation and piezoelectric properties of atom-thick α-M_2X_3 (M = Ga, In; X = S, Se): role of spontaneous electric dipole orientations, *RSC Adv.*, 2017, **7,** 55034-55043.

15 Y. Shen, Y. Guo and Q. Wang, Large out-of-plane second harmonic generation susceptibility in penta-ZnS_2 sheet, *Adv. Theory Simul.*, 2020, **3,** 2000027.

16 S. Zhang, J. Zhou, Q. Wang, X. Chen, Y. Kawazoe and P. Jena, Penta-graphene: a new carbon allotrope, *Proc. Natl. Acad. Sci. U.S.A.*, 2015, **112,** 2372-2377.

17 M. A. Nazir, A. Hassan, Y. Shen and Q. Wang, Research progress on penta-graphene and its related materials: Properties and applications, *Nano Today*, 2022, **44,** 101501.

18 Y. Shen and Q. Wang, Pentagon-based 2D materials: Classification, properties and applications, *Phys. Rep.* 2022, **964,** 1-42.

19 A. D. Oyedele, S. Yang, L. Liang, A. A. Puretzky, K. Wang, J. Zhang, P. Yu, P. R. Pudasaini, A. W. Ghosh, Z. Liu, C. M. Rouleau, B. G. Sumpter, M. F. Chisholm, W. Zhou, P. D. Rack, D. B. Geohegan and K. Xiao, $PdSe_2$: Pentagonal two-dimensional layers with high air stability for electronics, *J. Am. Chem. Soc.*, 2017, **139,** 14090-14097.

20 A. B. Puthirath, A. P. Balan, E. F. Oliveira, V. Sreepal, F. C. R. Hernandez, G. Gao, N. Chakingal, L. M. Sassi, P. Thibeorchews, G. Costin, R. Vajtai, D. S. Galvao, R. R. Nair and P. M. Ajayan, Apparent ferromagnetism in exfoliated ultrathin pyrite sheets, *J. Phys. Chem. C*, 2021, **125,** 18927-18935.

21 Y. Gu, H. Cai, J. Dong, Y. Yu, A. N. Hoffman, C. Liu, A. D. Oyedele, Y. C. Lin, Z. Ge, A. A. Puretzky, G. Duscher, M. F. Chisholm, P. D. Rack, C. M. Rouleau, Z. Gai, X. Meng, F. Ding, D. B. Geohegan and K. Xiao, Two-dimensional palladium diselenide with strong in-plane optical anisotropy and high mobility grown by chemical vapor deposition, *Adv. Mater.*, 2020, **32,** 1906238.

22 E. Li, D. Wang, P. Fan, R. Zhang, Y. Y. Zhang, G. Li, J. Mao, Y. Wang, X. Lin, S. Du and H. J. Gao, Construction of bilayer $PdSe_2$ on epitaxial graphene, *Nano Res.*, 2018, **11,** 5858-5865.

23 J. I. Cerdá, J. Sławińska, G. L. Lay, A. C. Marele, J. M. G. Rodríguez and M. E. Dávila, Unveiling the pentagonal nature of perfectly aligned single and double strand Si nano-ribbons on Ag(110), *Nat. Commun.*, 2016, **7,** 13076.

24 X. Zhang, G. Su, J. Lu, W. Yang, W. Zhuang, K. Han, X. Wang, Y. Wan, X. Yu and P. Yang, Centimeter scale few-layer PdS_2: Fabrication and physical properties, *ACS Appl. Mater. Interfaces*, 2021, **13,** 43063-43074.

25 M. Bykov, E. Bykova, A. V. Ponomareva, F. Tasnádi, S. Chariton, V. B. Prakapenka, K. Glazyrin, J. S. Smith, M. F. Mahmood, I. A. Abrikosov and A. F. Goncharov, Realization of an ideal cairo tessellation in nickel diazenide NiN_2: High-pressure route to pentagonal 2D materials, *ACS Nano*, 2021, **15,** 13539-13546.

26 K. M. Ok, E. O. Chi and P. S. Halasyamani, Bulk characterization methods for non-centrosymmetric materials: Second-harmonic generation, piezoelectricity, pyroelectricity, and ferroelectricity, *Chem. Soc. Rev.*, 2006, **35,** 710-717.

27 C. Wu, X. Jiang, L. Lin, Y. Hu, T. Wu, Z. Lin, Z. Huang, M. G. Humphrey and C. Zhang, A congruent-melting mid-infrared nonlinear optical vanadate exhibiting strong second-harmonic generation, *Angew. Chem. Int. Ed.*, 2021, **60,** 22447-22453.

28 H. Yu, H. Wu, S. Pan, Z. Yang, X. Hou, X. Su, Q. Jing, K. R. Poeppelmeier and J. M. Rondinelli, $Cs_3Zn_6B_9O_{21}$: A chemically benign member of the KBBF family exhibiting the largest second harmonic generation response, *J. Am. Chem. Soc.*, 2014, **136,** 1264-1267.

29 C. Hu, B. Zhang, B. H. Lei, S. Pan and Z. Yang, Advantageous units in antimony sulfides: Exploration and design of infrared nonlinear optical materials, *ACS Appl. Mater. Interfaces*, 2018, **10,** 26413-26421.

30 Z. Xie, M. Mutailipu, G. He, G. Han, Y. Wang, Z. Yang, M. Zhang and S. Pan, A series of rare-earth borates $K_7MRE_2B_{15}O_{30}$ (M = Zn, Cd, Pb; RE = Sc, Y, Gd, Lu)

with Large Second Harmonic Generation Responses, *Chem. Mater.*, 2018, **30,** 2414-2423.

31 J. A. Brant, D. J. Clark, Y. S. Kim, J. I. Jang, J. H. Zhang and J. A. Aitken, Li_2CdGeS_4, A diamond-like semiconductor with strong second-order optical nonlinearity in the infrared and exceptional laser damage threshold, C*hem. Mater.*, 2014, **26,** 3045-3048.

32 X. Dong, L. Huang, H. Zeng, Z. Lin, K. M. Ok and G. Zou, High-performance sulfate optical materials exhibiting giant second harmonic generation and large birefringence, *Angew. Chem. Int. Ed.*, 2022, **134,** e202116790.

33 G. Kresse and J. Furthmüller, Efficient iterative schemes for ab initio total-energy calculations using a plane-wave basis set, *Phys. Rev. B*, 1996, **54,** 11169-11186.

34 P. E. Blöchl, Projector augmented-wave method, *Phys. Rev. B*, 1994, **50,** 17953-17979.

35 J. P. Perdew, K. Burke and M. Ernzerhof, Generalized gradient approximation made simple, *Phys. Rev. Lett.* 1996, **77,** 3865-3868.

36 J. Heyd, G. E. Scuseria and M. Ernzerhof, Hybrid functionals based on a screened coulomb potential, *J. Chem. Phys.* 2003, **118,** 8207-8215.

37 H. J. Monkhorst and J. D. Pack, Special points for brillouin-zone integrations, *Phys. Rev. B*, 1976, **13,** 5188-5192.

38 A. Togo, F. Oba and I. Tanaka, First-principles calculations of the ferroelastic transition between rutile-type and $CaCl_2$-type SiO_2 at high pressures, *Phys. Rev. B*, 2008, **78,** 134106.

39 C. Braga and K. P. Travis, A configurational temperature nosé-hoover thermostat, *J. Chem. Phys.*, 2005, **123,** 134101.

40 X. Wu, D. Vanderbilt and D. R. Hamann, Systematic treatment of displacements, strains, and electric fields in density-functional perturbation theory, *Phys. Rev. B*, 2005, **72,** 035105.

41 J. E. Sipe and E. Ghahramani, Nonlinear optical response of semiconductors in the independent-particle approximation, *Phys. Rev. B*, 1993, **48,** 11705-11722.

42 Z. Fang, J. Lin, R. Liu, P. Liu, Y. Li, X. Huang, K. Ding, L. Ning and Y. Zhang, Computational design of inorganic nonlinear optical crystals based on a genetic algorithm, *CrystEngComm*, 2014, **16,** 10569-10580.

43 S. N. Rashkeev and W. R. L. Lambrecht, Second-harmonic generation of I-III-$\mathbf{V}$ I_2 halcopyrite semiconductors: Effects of chemical substitutions, *Phys. Rev. B*, 2001, **63,** 165212.

44 Z. H. Levine and D. C. Allan, Calculation of the nonlinear susceptibility for optical second-harmonic generation in III-V semiconductors, *Phys. Rev. Lett.*, 1991, **66,** 41-44.

45 Q. J. Liu, Z. T. Liu, L. P. Feng and H. Tian, First-principles study of structural, elastic, electronic and optical properties of rutile GeO_2 and and α-quartz GeO_2, *Solid State Sci.*, 2010, **12,** 1748-1755.

46 G. W. Milton, D. J. Eyre and J. V. Mantese, Finite frequency range kramers-kronig relations: bounds on the dispersion, *Phys. Rev. Lett.*, 1997, **79,** 3062-3065.

47 G. Yang and S. P. Gao, A method to restore the intrinsic dielectric functions of 2D

materials in periodic calculations, *Nanoscale*, 2021, **13,** 17057-17067.
48 Y, Guo, J. Zhou, H. Xie, Y. Chen and Q. Wang, Screening transition metal-based polar pentagonal monolayers with large piezoelectricity and shift current, *NPJ Comput. Mater.*, 2022, **8,** 1-9.
49 J. Paier, R. Hirschl, M. Marsman and G. Kresse, The perdew-burke-ernzerhof exchange-correlation functional applied to the G2-1 test set using a plane-wave basis set, *J. Chem. Phys.*, 2005, **122,** 234102.
50 M. Hellenbrandt, The inorganic crystal structure database (ICSD) — Present and future, *Crystallogr. Rev.*, 2014, **10,** 17-22.
51 R. Zacharia, H. Ulbricht and T. Hertel, Interlayer cohesive energy of graphite from thermal desorption of polyaromatic hydrocarbons, *Phys. Rev. B*, 2004, **69,** 155406..
52 J. H. Jung, C. H. Park and J. Ihm, A rigorous method of calculating exfoliation energies from first principles, *Nano Lett.*, 2018, **18,** 2759-2765.
53 J. Li, X. Fan, Y. Wei and G. Chen, Penta-B_xN_y sheet: A density functional theory study of two-dimensional material, *Sci. Rep.*, 2016, **6,** 31840.
54 E. Cadelano, P. L. Palla, S. Giordano and L. Colombo, Elastic properties of hydrogenated graphene, *Phys. Rev. B*, 2010, **82,** 235414.
55 C. Lee, X. Wei, J. W. Kysar and J. Hone, Measurement of the elastic properties and intrinsic strength of monolayer graphene, *Science*, 2008, **321,** 385-388.
56 A. D. Becke and K. E. Edgecombe, A simple measure of electron localization in atomic and molecular systems, *J. Chem. Phys.*, 1990, **92,** 5397-5403.
57 G. Henkelman, A. Arnaldsson and H. Jónsson, A fast and robust algorithm for bader decomposition of charge density, *Comput. Mater. Sci.*, 2006, **36,** 354-360.
58 W. Tang, E. Sanville and G. Henkelman, A grid-based bader analysis algorithm without lattice bias, *J. Phys. Condens. Matter*, 2009, **21,** 084204.
59 Y. L Page and P. Saxe, Symmetry-general least-squares extraction of elastic data for strained materials from ab initio calculations of stress, *Phys. Rev. B*, 2002, **65,** 104104.
60 C. T. Chen, G. L. Wang, X. Y. Wang and Z. Y. Xu, Deep-UV nonlinear optical crystal $KBe_2BO_3F_2$—discovery, growth, optical properties and applications, *Appl. Phys. B*, 2009, **97,** 9-25.
61 S. Grimme, Semiempirical GGA-type density functional constructed with a long-range dispersion correction, *J. Comput. Chem.*, 2006, **27,** 1787-1799.
62 L. Q. Yang, X. M. Jiang and G. C. Guo, $LiGa_{0.54}In_{0.46}S_2$: A new infrared nonlinear optical material with large laser damage threshold designed by gallium substitution in $LiInS_2$, *Inorg. Chem. Commun.*, 2020, **115,** 107852.
63 T. V. Vu, A. A. Lavrentyev, B. V. Gabrelian, D. D. Vo, K. D. Pham, N. M. Denysyuk, L. I. Isaenko, A. Y. Tarasova and O. Y. Khyzhun, DFT study and XPS measurements elucidating the electronic and optical properties of KPb_2Cl_5, *Opt. Mater.*, 2020, **102,** 109793.
64 H. Lin, L. Chen, J. S. Yu, H. Chen and L. M. Wu, Infrared SHG materials CsM_3Se_6 (M = Ga/Sn, In/Sn): Phase matchability controlled by dipole moment of the asymmetric building unit, *Chem. Mater.* 2017, **29,** 499-503.

65 P. Makuła, M. Pacia and W. Macyk, How to correctly determine the band gap energy of modified semiconductor photocatalysts based on UV–Vis spectra, *J. Phys. Chem. Lett.*, 2018, **9,** 6814-6817.
66 N. S. Abraham and M. R. Shirts, Thermal gradient approach for the quasi-harmonic approximation and its application to improved treatment of anisotropic expansion, *J. Chem. Theory Comput.*, 2018, **14,** 5904-5919.